Geophys. J. Int. (1991) **105**, 241–252

Reflection/transmission coefficients and azimuthal anisotropy in marine seismic studies

Subhashis Mallick and L. Neil Frazer

Department of Geology and Geophysics, School of Ocean and Earth Science and Technology, University of Hawaii at Manoa, 2525 Correa Road, Honolulu, HI 96822, USA

Accepted 1990 October 31. Received 1990 October 31; in original form 1990 August 14

SUMMARY

We introduce two methods for inferring the direction of vertical fractures from marine seismic data. First we derive the necessary reflection and transmission coefficients for an interface between a liquid and an azimuthally anisotropic solid. Next we show that multicomponent ocean bottom seismometer data from surface airgun sources along two perpendicular shot lines can be rotated into the principal directions of azimuthal anisotropy to determine the orientation of vertical fractures. Finally we show that *P*-wave amplitude versus offset (AVO) depends on the orientation of the shot line with respect to the vertical fractures. Thus *P*-wave AVO can also be used to determine fracture orientation.

Key words: AVO, azimuthal anisotropy, fractures, marine seismic studies, reflection coefficients.

1 INTRODUCTION

Seismic anisotropy is a rapidly growing area of research because of its potential in differentiating subsurface rock types. An introduction to anisotropy, with a glossary of terms and much useful tutorial material, has been given by Winterstein (1990), and the textbooks by Auld (1973) give straightforward derivations of many fundamental results. Useful reviews of major conferences on seismic anisotropy, accompanied by many other papers on the subject, were given by Bamford & Crampin (1977), Crampin, Chesnokov & Hipkin (1984), Booth, Crampin & Chesnokov (1987) and Leary, Crampin & McEvilly (1990). Here we are largely concerned with frequency–wavenumber methods for calculating synthetic seismograms in anisotropic layered-earth models; particulars of the method used are given by Fryer & Frazer (1984, 1987), Mallick & Frazer (1987, 1988, 1990), Frazer (1988) and Frazer & Fryer (1989). Ray theory methods are a useful alternative to frequency–wavenumber methods because ray methods are usually much faster to compute although sometimes less accurate. Červený (1972), Shearer & Chapman (1988) and Gajewski & Pšenčík (1990) gave ray theory methods for anisotropic media. Chapman & Shearer (1988) pointed out fundamental difficulties in anisotropic ray theory caused by gradient zone coupling between shear rays of different type. References to other useful papers can be found in those just cited.

To generate effective elastic coefficients for fractured and microbedded rocks we use the Schoenberg method (Schoenberg 1983; Schoenberg & Douma 1988; Schoenberg & Muir 1989). An alternative method for fractures, but not for microbeds, is that of Hudson (1980, 1981, 1986, 1988, 1990a,b). The Hudson method assumes that the cracks are small in the sense that $\nu a^3 \ll 1$ where ν is the number of cracks per unit volume and a is the mean radius of the cracks, whereas the Schoenberg method assumes that the cracks are infinite. The Schoenberg method is quasistatic, so that multiple reflections between fractures do not contribute to the attenuation. Although the Hudson method is dynamic, Hudson (1990b) has also shown that his effective elastic coefficients contain no attenuation component due to scattering. The Hudson and Schoenberg methods are equivalent in the sense that parameters in either method can be found which give the same anisotropy (Schoenberg & Douma 1988). At this time we prefer the Schoenberg method because it gives a unified treatment of microbeds and fractures, because it can be used iteratively—for example, a microbedded or fractured rock can be microbedded or fractured again in a different direction, and because the mathematics on which it is based are very straightforward. More discussion of the differences between the Schoenberg and Hudson methods can be found in Mallick & Frazer (1990) and Frazer (1990).

In this paper the abbreviation TI means transversely isotropic with a vertical symmetry axis, and AA means azimuthal anisotropy. A TI medium is thus one in which soundspeeds vary with angle to the vertical, but not with azimuth. An AA medium is one in which soundspeeds vary with azimuth as well as angle to the vertical. The abbreviation AI means azimuthally isotropic, that is, either isotropic or TI.

Computing plane-wave reflection and transmission (R/T) coefficients at boundaries is one of the fundamental problems of computational seismology. For liquids and isotropic solids the solutions are well known (e.g. Aki & Richards 1980). Fryer & Frazer (1984) give the general form of the R/T coefficients for anisotropic layers, but their results are valid only for solid–solid interfaces. As R/T coefficients for anisotropic solid–liquid layer boundaries are not presently available, existing computer codes for AA media are not useful for marine data. This paper shows how to compute R/T coefficients for liquid–liquid, liquid–solid, and solid–liquid interfaces in an AA modelling code. These results are then used to develop two methods of determining fracture orientation from seismic data.

2 R/T COEFFICIENTS

We work in a right-handed Cartesian coordinate system, x, y, z with the z-axis pointing vertically downwards. We assume a stratified earth so that the material properties depend only on depth z. Accordingly, we Fourier transform from time t to temporal frequency ω and from range coordinates (x, y) to horizontal slownesses (p_x, p_y). In the sequel all field variables are thus functions of ω, p_x, p_y, and z. Bold-face lower case letters are used to denote vectors and bold-face upper case letters are used to denote matrices. In the problem of reflection and transmission at depth $z = z_1$, we use the notations z_1^- and z_1^+ to denote depths just above and just below the inferface, respectively.

For the problem of reflection and transmission between two anisotropic layers at $z = z_1$ (Fig. 1), we distinguish two cases: (1) a downgoing wavefield incident from above (Fig. 1a), and (2) an upgoing wavefield incident from below (Fig. 1b). In the notation of Kennett (1983), and of Fryer & Frazer (1984), we have, for case 1:

$$\begin{pmatrix} \mathbf{0} \\ \mathbf{v}_d(z_1^+) \end{pmatrix} = \mathbf{Q}(z_1^+, z_1^-) \begin{pmatrix} \mathbf{v}_u(z_1^-) \\ \mathbf{v}_d(z_1^-) \end{pmatrix}, \tag{1}$$

and for case 2:

$$\begin{pmatrix} \mathbf{v}_u(z_1^+) \\ \mathbf{v}_d(z_1^+) \end{pmatrix} = \mathbf{Q}(z_1^+, z_1^-) \begin{pmatrix} \mathbf{v}_u(z_1^-) \\ \mathbf{0} \end{pmatrix}. \tag{2}$$

Here $\mathbf{v}_u(z_1^-)$ and $\mathbf{v}_d(z_1^-)$ are the up- and downgoing wave vectors, respectively, just above the interface and $\mathbf{v}_u(z_1^+)$ and $\mathbf{v}_d(z_1^+)$ are the up- and downgoing wave vectors, respectively, just below the interface. In AA media we speak of the quasi-P-wave, denoted by q_P, and the two quasi-shear waves, denoted by q_{S_1} and q_{S_2}. The components of the wave vectors are the amplitudes of the waves; for example,

$$\mathbf{v}_u(z_1^+) = [v_u^P(z_1^+),\ v_u^{S_1}(z_1^+),\ v_u^{S_2}(z_1^+)]^T, \tag{3}$$

where $v_u^P(z_1^+)$, $v_u^{S_1}(z_1^+)$, and $v_u^{S_2}(z_1^+)$ are the respective amplitudes of the upgoing q_P-, q_{S_1}-, and q_{S_2}-waves at $z = z_1^+$. In equations (1) and (2) the 6×6 downward wave propagator matrix $\mathbf{Q}$ can be expressed in terms of the eigenvector matrices $\mathbf{D}$ for the layers above and below the interface (see Fryer & Frazer 1984) as

$$\mathbf{Q}(z_1^+, z_1^-) = \mathbf{D}^{-1}(z_1^+)\mathbf{D}(z_1^-). \tag{4}$$

At the interface z_1, the downgoing wavefield $\mathbf{v}_d(z_1^-)$ in Fig. 1(a) generates the reflected wavefield $\mathbf{v}_u(z_1^-)$ and the transmitted wavefield $\mathbf{v}_d(z_1^+)$. Therefore the wavevectors in equation (1) are related by the downward looking R/T matrices $\mathbf{R}_d$ and $\mathbf{T}_d$ as

$$\mathbf{v}_u(z_1^-) = \mathbf{R}_d\mathbf{v}_d(z_1^-), \tag{5}$$

and

$$\mathbf{v}_d(z_1^+) = \mathbf{T}_d\mathbf{v}_d(z_1^-). \tag{6}$$

Similarly, the upgoing wavefield $\mathbf{v}_u(z_1^+)$ in Fig. 1(b) generates the reflected wavefield $\mathbf{v}_d(z_1^+)$ and the transmitted wavefield $\mathbf{v}_u(z_1^-)$. Therefore the wavevectors in equation (2) are related by the upward looking R/T matrices $\mathbf{R}_u$ and $\mathbf{T}_u$ as

$$\mathbf{v}_d(z_1^+) = \mathbf{R}_u\mathbf{v}_u(z_1^+), \tag{7}$$

and

$$\mathbf{v}_u(z_1^-) = \mathbf{T}_u\mathbf{v}_u(z_1^+). \tag{8}$$

The last four equations can be regarded as definitions of $\mathbf{R}_d$, $\mathbf{T}_d$, $\mathbf{R}_u$, and $\mathbf{T}_u$. In terms of components, $\mathbf{R}_d$ is written as

$$\mathbf{R}_d = \begin{pmatrix} r_{PP}^d & r_{P1}^d & r_{P2}^d \\ r_{1P}^d & r_{11}^d & r_{12}^d \\ r_{2P}^d & r_{21}^d & r_{22}^d \end{pmatrix},$$

where r_{1P}^d is the amplitude of an upward q_{S_1}-wave generated by reflection of a downward incident q_P-wave of unit amplitude, and so on. Components of the other R/T matrices are ordered similarly. To obtain $\mathbf{R}_d$, $\mathbf{T}_d$, $\mathbf{R}_u$, and $\mathbf{T}_u$ from equations (1) and (2) above, first let $\mathbf{Q}_{11}$, $\mathbf{Q}_{12}$, $\mathbf{Q}_{21}$, and $\mathbf{Q}_{22}$ be the 3×3 submatrices of the 6×6 wave propagator matrix $\mathbf{Q}$:

$$\mathbf{Q} = \begin{pmatrix} \mathbf{Q}_{11} & \mathbf{Q}_{12} \\ \mathbf{Q}_{21} & \mathbf{Q}_{22} \end{pmatrix}. \tag{9}$$

Then for a solid–solid interface we have the well-known relations (e.g. Kennett 1983; Fryer & Frazer 1984):

$$\mathbf{T}_u = \mathbf{Q}_{11}^{-1}, \tag{10}$$

$$\mathbf{R}_d = -\mathbf{Q}_{11}^{-1}\mathbf{Q}_{12}, \tag{11}$$

$$\mathbf{R}_u = \mathbf{Q}_{21}\mathbf{Q}_{11}^{-1}, \tag{12}$$

$$\mathbf{T}_d = \mathbf{Q}_{22} - \mathbf{Q}_{21}\mathbf{Q}_{11}^{-1}\mathbf{Q}_{12}. \tag{13}$$

The definition of the wave propagator $\mathbf{Q}$ by equation (4) is based on a solid–solid boundary condition, i.e., the displacement and the normal traction are continuous across the interface. For liquids, only the vertical component of the displacement and the vertical component of normal traction

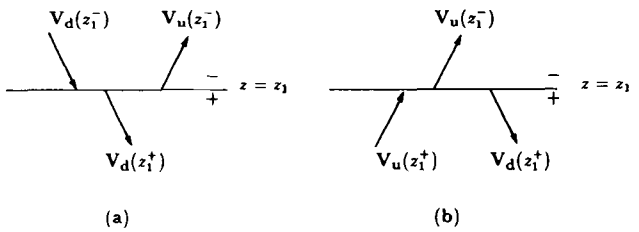

Figure 1. Reflection and transmission problem in seismology. (a) Wavefield incident from above, and (b) wavefield incident from below.

are continuous across the boundary and the other two components of the normal traction vanish at the boundary. Therefore equation (4) is not meaningful for liquids; equations (10)–(13) cannot be used for computing the R/T coefficient matrices for liquid layers, because for a liquid the $\mathbf{Q}_{11}$ submatrix of $\mathbf{Q}$ in equation (9) is singular.

To find R/T coefficients for liquids, we examine the definition of the $\mathbf{D}$ matrix and the appropriate boundary conditions. In a solid, the first three columns of $\mathbf{D}$ represent upgoing q_P-, q_{S_1}-, and q_{S_2}-waves while the last three columns represent downgoing q_P-, q_{S_1}-, and q_{S_2}-waves. The columns of $\mathbf{D}$ are the displacement–stress vectors $\mathbf{b}$ for each of the six wave types. These displacement–stress vectors $\mathbf{b}$ have the form (after normalization)

$$\mathbf{b} = (\mathbf{u}, \mathbf{t})^{\mathrm{T}}, \tag{14}$$

where $\mathbf{u}$ is the displacement vector:

$$\mathbf{u} = (u_x, u_y, u_z)^{\mathrm{T}}, \tag{15}$$

and $\mathbf{t}$ is a vector proportional to the vector of vertical tractions:

$$\mathbf{t} = -\frac{1}{i\omega}(\tau_{zx}, \tau_{zy}, \tau_{zz})^{\mathrm{T}}. \tag{16}$$

For a liquid, the q_{S_1}-, and q_{S_2}-waves do not exist and therefore the second, third, fifth, and sixth columns of $\mathbf{D}$ are zeroes. Also, for liquids, only the normal stress τ_{zz} exists while the shear stresses τ_{zx}, and τ_{zy} are always zero. Therefore the fourth and fifth rows of $\mathbf{D}$ are all zeroes. Therefore the eigenvector matrix $\mathbf{D}$ for a liquid has the form

$$\mathbf{D} = \begin{pmatrix} D_{11} & 0 & 0 & D_{14} & 0 & 0 \\ D_{21} & 0 & 0 & D_{24} & 0 & 0 \\ D_{31} & 0 & 0 & D_{34} & 0 & 0 \\ 0 & 0 & 0 & 0 & 0 & 0 \\ 0 & 0 & 0 & 0 & 0 & 0 \\ D_{61} & 0 & 0 & D_{64} & 0 & 0 \end{pmatrix}. \tag{17}$$

We now consider the liquid–liquid, liquid–solid, and solid–liquid reflection problems separately.

2.1 Liquid–liquid case

For a liquid-over-liquid interface, the boundary conditions are

$$u_z(z_1^-) = u_z(z_1^+), \tag{18}$$

$$\tau_{zz}(z_1^-) = \tau_{zz}(z_1^+), \tag{19}$$

$$\tau_{zx}(z_1^-) = \tau_{zx}(z_1^+) = 0, \tag{20}$$

and

$$\tau_{zy}(z_1^-) = \tau_{zy}(z_1^+) = 0. \tag{21}$$

Note that the displacement–stress vector $\mathbf{b}$, defined by equation (14) is related to the wavevector $\mathbf{v} = (\mathbf{v}_u, \mathbf{v}_d)^{\mathrm{T}}$ by $\mathbf{b} = \mathbf{D}\mathbf{v}$. Also note that the $\mathbf{D}$ matrix for liquids is given by equation (17). Thus, for the wavefield incident from above (Fig. 1a), our boundary conditions become

$$D_{31}(z_1^-)v_u^P(z_1^-) + D_{34}(z_1^-)v_d^P(z_1^-) = D_{34}(z_1^+)v_d^P(z_1^+), \tag{22}$$

and

$$D_{61}(z_1^-)v_u^P(z_1^-) + D_{64}(z_1^-)v_d^P(z_1^-) = D_{64}(z_1^+)v_d^P(z_1^+). \tag{23}$$

From equations (22) and (23) and the definitions of the downward looking reflection and transmission coefficients $\mathbf{R}_d$ and $\mathbf{T}_d$, given by equations (5) and (6), it follows that

$$\mathbf{R}_d = \begin{pmatrix} r_{PP}^d & 0 & 0 \\ 0 & 0 & 0 \\ 0 & 0 & 0 \end{pmatrix}, \tag{24}$$

and

$$\mathbf{T}_d = \begin{pmatrix} t_{PP}^d & 0 & 0 \\ 0 & 0 & 0 \\ 0 & 0 & 0 \end{pmatrix}, \tag{25}$$

in which

$$r_{PP}^d = \frac{D_{64}(z_1^-)D_{34}(z_1^+) - D_{34}(z_1^-)D_{64}(z_1^+)}{D_{31}(z_1^-)D_{64}(z_1^+) - D_{61}(z_1^-)D_{34}(z_1^+)}, \tag{26}$$

and

$$t_{PP}^d = \frac{D_{31}(z_1^-)D_{64}(z_1^-) - D_{61}(z_1^-)D_{34}(z_1^-)}{D_{31}(z_1^-)D_{64}(z_1^+) - D_{61}(z_1^-)D_{34}(z_1^+)}. \tag{27}$$

Similarly, for the wavefield incident from below (Fig. 1b), the boundary conditions,

$$D_{31}(z_1^+)v_u^P(z_1^+) + D_{34}(z_1^+)v_d^P(z_1^+) = D_{31}(z_1^-)v_u^P(z_1^-),$$
$$D_{61}(z_1^+)v_u^P(z_1^+) + D_{64}(z_1^+)v_d^P(z_1^+) = D_{61}(z_1^-)v_u^P(z_1^-),$$

and the definitions of $\mathbf{R}_u$ and $\mathbf{T}_u$ by equations (7) and (8), give

$$\mathbf{R}_u = \begin{pmatrix} r_{PP}^u & 0 & 0 \\ 0 & 0 & 0 \\ 0 & 0 & 0 \end{pmatrix}, \tag{28}$$

and

$$\mathbf{T}_u = \begin{pmatrix} t_{PP}^u & 0 & 0 \\ 0 & 0 & 0 \\ 0 & 0 & 0 \end{pmatrix}, \tag{29}$$

in which

$$r_{PP}^u = \frac{D_{61}(z_1^+)D_{31}(z_1^-) - D_{31}(z_1^+)D_{61}(z_1^-)}{D_{34}(z_1^+)D_{61}(z_1^-) - D_{64}(z_1^+)D_{31}(z_1^-)}, \tag{30}$$

and

$$t_{PP}^u = \frac{D_{34}(z_1^+)D_{61}(z_1^+) - D_{64}(z_1^+)D_{31}(z_1^+)}{D_{34}(z_1^+)D_{61}(z_1^-) - D_{64}(z_1^+)D_{31}(z_1^-)}. \tag{31}$$

This completes the solution for the upward- and downward-looking R/T coefficients in the liquid-over-liquid case. Corresponding results in the context of the 4×4 PSV system have been given by Kennett (1983, p. 157).

2.2 Liquid–solid case

For the liquid-over-solid case, the boundary conditions are

$$\begin{pmatrix} u_z(z_1^-) \\ 0 \\ 0 \\ \tau_{zz}(z_1^-) \end{pmatrix} = \begin{pmatrix} u_z(z_1^+) \\ \tau_{zx}(z_1^+) \\ \tau_{zy}(z_1^+) \\ \tau_{zz}(z_1^+) \end{pmatrix}. \tag{32}$$

Recall that the **D** matrix for a liquid is given by equation (17). Also, write the **D** matrix for a solid in terms of its 3×3 submatrices as

$$\mathbf{D} = \begin{pmatrix} \mathbf{M}_u & \mathbf{M}_d \\ \mathbf{N}_u & \mathbf{N}_d \end{pmatrix}. \tag{33}$$

Again the displacement–stress vector **b** defined by equation (14) is related to the wavevector **v** by $\mathbf{b} = \mathbf{D}\mathbf{v}$. Thus, for the wavefield incident from above (Fig. 1a), the continuity of vertical motion in equation (32) may be expressed in terms of **v** as

$$D_{31}(z_1^-)v_u^P(z_1^-) + D_{34}(z_1^-)v_d^P(z_1^-) = \mathbf{d}_1^{\mathrm{T}}\mathbf{v}_d(z_1^+) \tag{34}$$

where

$$\mathbf{d}_1 = [D_{34}(z_1^+), D_{35}(z_1^+), D_{36}(z_1^+)]^{\mathrm{T}} \tag{35}$$

and the continuity of the tractions in equation (32) becomes

$$\begin{pmatrix} 0 \\ 0 \\ D_{61}(z_1^-)v_u^P(z_1^-) + D_{64}(z_1^-)v_d^P(z_1^-) \end{pmatrix} = \mathbf{N}_d(z_1^+)\mathbf{v}_d(z_1^+). \tag{36}$$

Equation (36) can be simplified to

$$\mathbf{v}_d(z_1^+) = \mathbf{x}[D_{61}(z_1^-)v_u^P(z_1^-) + D_{64}(z_1^-)v_d^P(z_1^-)], \tag{37}$$

where

$$\mathbf{x} = \{[\mathbf{N}_d^{-1}(z_1^+)]_{13}, [\mathbf{N}_d^{-1}(z_1^+)]_{23}, [\mathbf{N}_d^{-1}(z_1^+)]_{33}\}^{\mathrm{T}}. \tag{38}$$

Substitution of equation (37) into (34) and using the definition of $\mathbf{R}_d$ given in equation (5) gives, after some algebra:

$$\mathbf{R}_d = \begin{pmatrix} r_{PP}^d & 0 & 0 \\ 0 & 0 & 0 \\ 0 & 0 & 0 \end{pmatrix}, \tag{39}$$

in which

$$r_{PP}^d = \frac{D_{34}(z_1^-) - (\mathbf{d}_1^{\mathrm{T}}\mathbf{x})D_{64}(z_1^-)}{(\mathbf{d}_1^{\mathrm{T}}\mathbf{x})D_{61}(z_1^-) - D_{31}(z_1^-)}. \tag{40}$$

Next, dividing both sides of (37) by $v_d^P(z_1^-)$ and substituting (40) into the result yields from the definition of $\mathbf{T}_d$ in equation (6)

$$\mathbf{T}_d = \begin{pmatrix} t_{PP}^d & 0 & 0 \\ t_{1P}^d & 0 & 0 \\ t_{2P}^d & 0 & 0 \end{pmatrix}, \tag{41}$$

in which

$$(t_{PP}^d, t_{1P}^d, t_{2P}^d)^{\mathrm{T}} = m\mathbf{x}, \tag{42}$$

where

$$m = \frac{D_{61}(z_1^-)D_{34}(z_1^-) - D_{64}(z_1^-)D_{31}(z_1^-)}{(\mathbf{d}_1^{\mathrm{T}}\mathbf{x})D_{61}(z_1^-) - D_{31}(z_1^-)}. \tag{43}$$

Now, for the wavefield incident from below (Fig. 1b), the continuity of the vertical component of motion in equation (32), and the relation $\mathbf{b} = \mathbf{D}\mathbf{v}$ demand that

$$D_{31}(z_1^-)v_u^P(z_1^-) = \mathbf{d}_2\mathbf{v}_u(z_1^+) + \mathbf{d}_1\mathbf{v}_d(z_1^+), \tag{44}$$

where $\mathbf{d}_1$ is defined in equation (35), and $\mathbf{d}_2$ is given by

$$\mathbf{d}_2 = [D_{31}(z_1^+), D_{32}(z_1^+), D_{33}(z_1^+)]^{\mathrm{T}}. \tag{45}$$

Similarly, the continuity of the normal traction in (32) and the relation $\mathbf{b} = \mathbf{D}\mathbf{v}$ give

$$\begin{pmatrix} 0 \\ 0 \\ D_{61}(z_1^-)v_u^P(z_1^-) \end{pmatrix} = \mathbf{N}_u(z_1^+)\mathbf{v}_u(z_1^+) + \mathbf{N}_d(z_1^+)\mathbf{v}_d(z_1^+). \tag{46}$$

Equation (46) can be further simplified as

$$\mathbf{v}_d(z_1^+) = \mathbf{x}D_{61}(z_1^-)v_u^P(z_1^-) - \mathbf{N}_d^{-1}(z_1^+)\mathbf{N}_u(z_1^+)\mathbf{v}_u(z_1^+), \tag{47}$$

where **x** is defined above in equation (38). Substitution of equation (43) into (44) and use of the definitions of $\mathbf{R}_u$ and $\mathbf{T}_u$ given in equations (7) and (8), respectively, gives after some algebra:

$$\mathbf{T}_u = \begin{pmatrix} t_{PP}^u & t_{P1}^u & t_{P2}^u \\ 0 & 0 & 0 \\ 0 & 0 & 0 \end{pmatrix}, \tag{48}$$

and

$$\mathbf{R}_u = D_{61}(z_1^-)\mathbf{x}^{\mathrm{T}}(t_{PP}^u, t_{P1}^u, t_{P2}^u) - \mathbf{B}, \tag{49}$$

in which

$$(t_{PP}^u, t_{P1}^u, t_{P2}^u) = \frac{1}{n}(\mathbf{d}_1^{\mathrm{T}}\mathbf{B} - \mathbf{d}_2^{\mathrm{T}}), \tag{50}$$

$$\mathbf{B} = \mathbf{N}_d^{-1}(z_1^+)\mathbf{N}_u(z_1^+), \tag{51}$$

and

$$n = (\mathbf{d}_1^{\mathrm{T}}\mathbf{x})D_{61}(z_1^-) - D_{31}(z_1^-). \tag{52}$$

This completes the solution for the liquid–solid case.

2.3 Solid–liquid case

For the solid-over-liquid interface we proceed similarly to the liquid-over-solid interface to obtain

$$\mathbf{R}_u = \begin{pmatrix} r_{PP}^u & 0 & 0 \\ 0 & 0 & 0 \\ 0 & 0 & 0 \end{pmatrix}, \tag{53}$$

$$\mathbf{T}_u = \begin{pmatrix} t_{PP}^u & 0 & 0 \\ t_{1P}^u & 0 & 0 \\ t_{2P}^u & 0 & 0 \end{pmatrix}, \tag{54}$$

$$\mathbf{T}_d = \begin{pmatrix} t_{PP}^d & t_{P1}^d & t_{P2}^d \\ 0 & 0 & 0 \\ 0 & 0 & 0 \end{pmatrix}, \tag{55}$$

and

$$\mathbf{R}_d = D_{64}(z_1^+)\mathbf{y}^{\mathrm{T}}(t_{PP}^d, t_{P1}^d, t_{P2}^d) - \mathbf{F}. \tag{56}$$

In equations (53)–(56) above,

$$r_{PP}^u = \frac{D_{31}(z_1^+) - (\mathbf{d}_4^{\mathrm{T}}\mathbf{y})D_{61}(z_1^+)}{(\mathbf{d}_4^{\mathrm{T}}\mathbf{y})D_{64}(z_1^+) - D_{34}(z_1^+)}, \tag{57}$$

$$(t_{PP}^u, t_{1P}^u, t_{2P}^u)^{\mathrm{T}} = m\mathbf{y}, \tag{58}$$

$$(t_{PP}^d, t_{P1}^d, t_{P2}^d) = \frac{1}{n}(\mathbf{d}_4^{\mathrm{T}}\mathbf{F} - \mathbf{d}_3^{\mathrm{T}}), \tag{59}$$

Table 1. Model used to compute the synthetic seismograms shown in Figs 3, 4, and 5.

Layer No.	Elastic Coefficient Matrix (10^9N m^{-2})	Density (kg m^{-3})	Q	Thickness (m)
1	$\begin{pmatrix} 2.25 & 2.25 & 2.25 & 0 & 0 & 0 \\ 2.25 & 2.25 & 2.25 & 0 & 0 & 0 \\ 2.25 & 2.25 & 2.25 & 0 & 0 & 0 \\ 0 & 0 & 0 & 0 & 0 & 0 \\ 0 & 0 & 0 & 0 & 0 & 0 \\ 0 & 0 & 0 & 0 & 0 & 0 \end{pmatrix}$	1000	1000	500
2	$\begin{pmatrix} 7.921 & 2.396 & 2.315 & 0 & 0 & 0 \\ 2.396 & 8.540 & 2.264 & 0 & 0 & 0 \\ 2.135 & 2.264 & 6.949 & 0 & 0 & 0 \\ 0 & 0 & 0 & 2.25 & 0 & 0 \\ 0 & 0 & 0 & 0 & 2.153 & 0 \\ 0 & 0 & 0 & 0 & 0 & 2.83 \end{pmatrix}$	1750	250	500
3	$\begin{pmatrix} 49.000 & 16.370 & 16.260 & 0 & 0 & 0 \\ 16.370 & 31.360 & 16.370 & 0 & 0 & 0 \\ 16.260 & 16.370 & 49.000 & 0 & 0 & 0 \\ 0 & 0 & 0 & 10.459 & 0 & 0 \\ 0 & 0 & 0 & 0 & 16.370 & 0 \\ 0 & 0 & 0 & 0 & 0 & 10.459 \end{pmatrix}$	1960	250	500
4	$\begin{pmatrix} 47.193 & 16.389 & 17.867 & 0 & 0 & 0 \\ 16.389 & 43.536 & 16.389 & 0 & 0 & 0 \\ 17.867 & 16.389 & 47.193 & 0 & 0 & 0 \\ 0 & 0 & 0 & 14.045 & 0 & 0 \\ 0 & 0 & 0 & 0 & 14.663 & 0 \\ 0 & 0 & 0 & 0 & 0 & 14.045 \end{pmatrix}$	2425	250	Half Space

where

$$\mathbf{y} = \{[\mathbf{N}_u^{-1}(z_1^-)]_{13}, [\mathbf{N}_u^{-1}(z_1^-)]_{23}, [\mathbf{N}_u^{-1}(z_1^-)]_{33}\}^T, \tag{60}$$

$$m = \frac{D_{64}(z_1^+)D_{31}(z_1^+) - D_{61}(z_1^+)D_{34}(z_1^+)}{(\mathbf{d}_4^T\mathbf{y})D_{64}(z_1^+) - D_{34}(z_1^+)}, \tag{61}$$

$$\mathbf{F} = \mathbf{N}_u^{-1}(z_1^-)\mathbf{N}_d(z_1^-), \tag{62}$$

$$n = (\mathbf{d}_4^T\mathbf{y})D_{64}(z_1^+) - D_{34}(z_1^+), \tag{63}$$

$$\mathbf{d}_3 = [D_{34}(z_1^-), D_{35}(z_1^-), D_{36}(z_1^-)]^T, \tag{64}$$

and

$$\mathbf{d}_4 = [D_{31}(z_1^-), D_{32}(z_1^-), D_{33}(z_1^-)]^T. \tag{65}$$

We now have complete expressions for the R/T coefficients for interfaces between liquids and AA solids. Numerous test computations, some of which are shown in the next section, indicate that the use of these expressions is far more robust than simulating a liquid by setting the rigidity to a very small number and using solid–solid R/T coefficients. As in isotropic media, singularities of the liquid–solid and solid–liquid R/T coefficients correspond to Scholte waves (Stonely waves).

3 EXAMPLES

Here we give three examples. The model used to compute all the examples is described in Table 1. The model consists of a 500 m thick water layer, overlying two 500 m thick AA layers and an AA half-space. Layer 2 of this model was taken from Schoenberg, Mallick & Frazer (1988) and represents a vertically fractured TI medium. Layers 3 and 4 of the model were taken respectively from Stephen (1985, fig. 4, with the values of C_{44} and C_{66} interchanged) and Mallick & Frazer (1990, table 4) and each of them represents a vertically fractured isotropic medium.

In Figs 3, 4 and 5 the source was an explosion 10 m below the top of the water layer, and the source time-function was an impulse response band limited by a frequency-domain

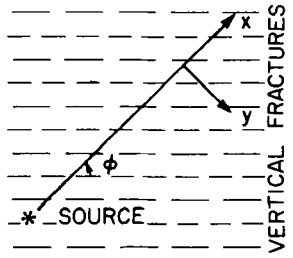

Figure 2. Orientation of vertical fractures with respect to the seismic profiles shown in Figs 3, 4, and 5.

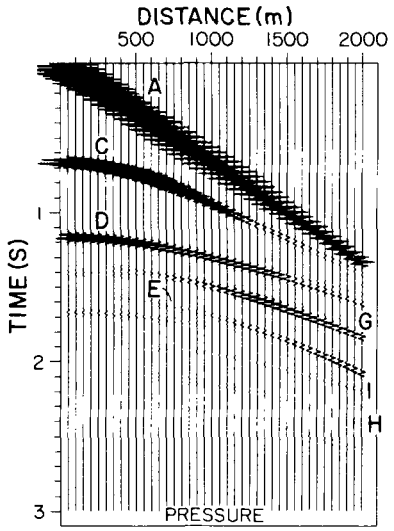

Figure 3. Synthetic pressure response computed at the surface of the water layer, using the model shown in Table 1. The events marked are as follows: (A) direct P arrival, (C) P reflection from the ocean bottom, (D) q_P reflection from the top of layer 3, (E) q_{S_1} reflection from the top of layer 3, (G) q_P reflection from the top of layer 4, (H) q_{S_1} reflection from the top of layer 4, and (I) q_{S_2} reflection from the top of layer 4.

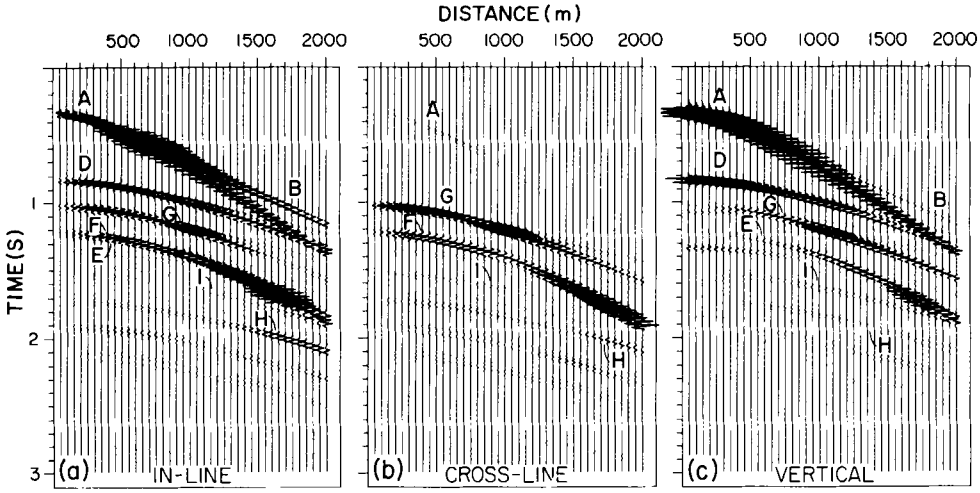

Figure 4. (a) x-, (b) y-, and (c) z-components of motion for receivers located at the ocean bottom with source in the water, for the model given in Table 1. Events marked are as follows: (A) direct P arrival, (B) head wave, (D) q_P reflection from the top of layer 3, (E) q_{S_1} reflection from the top of layer 3, (F) q_{S_2} reflection from the top of layer 3, (G) q_P reflection from the top of layer 4, (H) q_{S_1} reflection from the top of layer 4, and (I) q_{S_2} reflection from the top of layer 4.

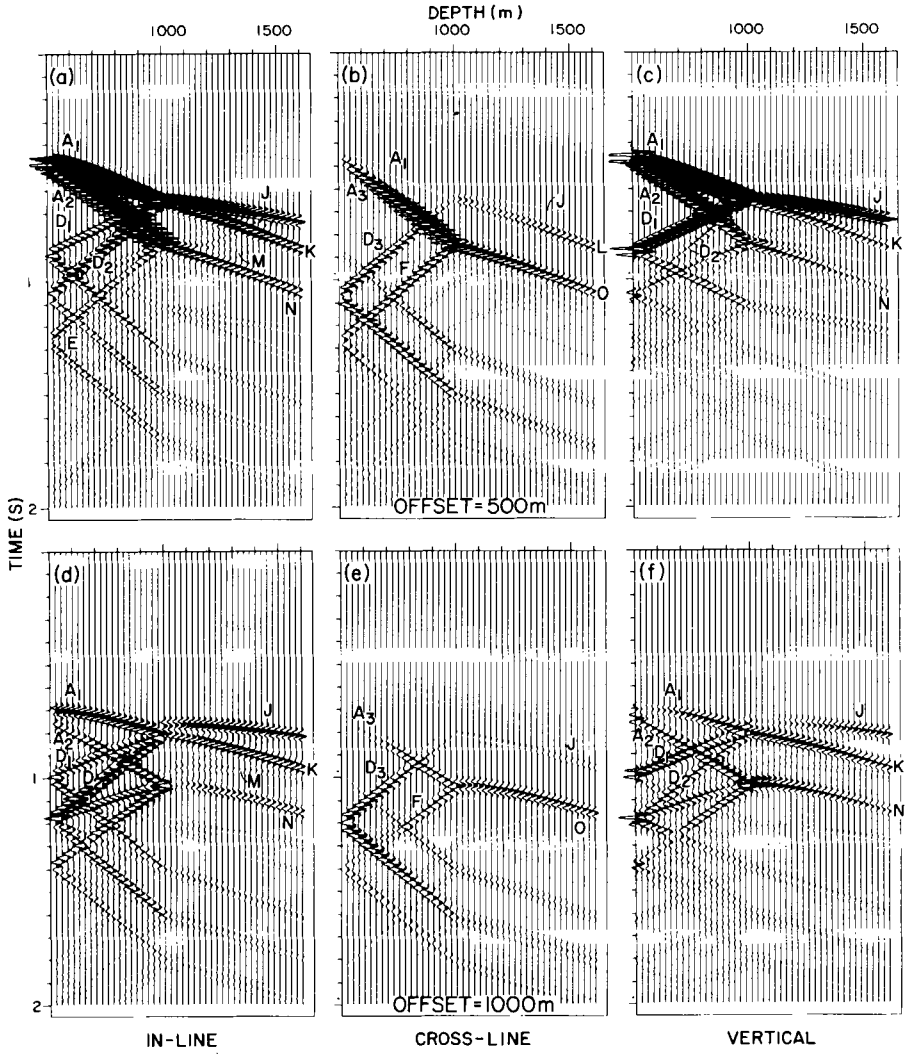

Figure 5. (a) x-, (b) y-, and (c) z-components of VSP response at a horizontal offset of 500 m, computed using the model given in Table 1. (d), (e), (f) same as (a), (b), (c), but for a horizontal offset of 1000 m. Events marked are as follows: (A_1) q_P, (A_2) q_{S_1}, (A_3) q_{S_2}, (D_1) q_P–q_P reflection from top of layer 3, (D_2) q_P–q_{S_1} reflection from top of layer 3, (D_3) q_P–q_{S_2} reflection from top of layer 3, (E) q_{S_1}–q_{S_1} reflection from the top of layer 3, (F) q_{S_2}–q_{S_2} reflection from the top of layer 3, (J) transmitted q_P–q_P into layer 3, (K) transmitted q_P–q_{S_1} into layer 3, (L) transmitted q_P–q_{S_2} into layer 3, (M) transmitted q_{S_1}–q_P into layer 3, (N) transmitted q_{S_1}–q_{S_1} into layer 3, (O) transmitted q_{S_2}–q_{S_2} into layer 3.

Hanning window between 10 and 60 Hz. In Figs 3 and 4 the ray parameter aperture was $-1.0 \le p_x$, $p_y \le 1.0$ with 600 values of p_x and 600 values of p_y. For the VSP in Fig. 5 the ray parameter aperture was reduced to $-0.61 \le p_x$, $p_y \le 0.61$ with 150 values of p_x and 150 values of p_y. The synthetic seismograms were computed using the ANIVEC^{TM}* software (Mallick & Frazer 1990). In order to simplify the interpretation of the synthetic seismograms, the effects of the free surface were excluded from the computation.

The first example (Fig. 3) shows the pressure response at the surface, along a line at $\phi = 45°$ to the strike of the fractures (see Fig. 2). The second example (Fig. 4a–c) shows the x-, y-, and z-components of motion for receivers located on the ocean bottom, along a line at $\phi = 45°$ to the strike of the vertical fractures. The third example (Fig. 5a–f) consists of offset VSPs for the same model (Table 1). The x-, y-, and z-components of motion are shown for depths of 500 to 1600 m, at horizontal offsets of 500 m (Fig. 5a–c) and 1000 m (Fig. 5d–f), for an angle of $\phi = 45°$.

The phases identified on the synthetics in Figs 3, 4, and 5 show many characteristic features of wave propagation in AA media. For example, in Fig. 3, note the different arrival times for the q_{S_1} and q_{S_2} reflections from the top of layer 4 (phases marked as H and I respectively). In AA media, the two quasi-shear waves q_{S_1} and q_{S_2} travel with different wavespeeds giving rise to the phenomenon known as shear-wave splitting. In Fig. 4, the y-component of the response (Fig. 4*b*) would have been zero if the medium were AI. Here too, the shear-wave splitting is apparent in reflections from the top of layer 3 (events E and F) and in reflections from the top of layer 4 (events H and I). Finally, in Fig. 5, we see shear-wave splitting in the events K and L, and N and O. In Fig. 5 also, the y-component of the responses (Figs. 5b and 5e) would have been zero if the medium were AI.

4 FRACTURE ORIENTATION FROM MARINE AIRGUN-OBS DATA

The synthetic examples in Figs 3, 4, and 5 indicate that for marine seismic exploration, multicomponent offset VSP is the best method for an unambiguous detection of azimuthal anisotropy. For example, the splitting in layer 3, indicated by events H and I in Figs 3 and 4, might easily be misinterpreted as reflections from two different layers or as multiple reflections. But in the VSP examples of Fig. 5, the transmitted events K and L, and N and O demonstrate that H and I are actually reflections from the same interface. Although offset VSP is a good method for detection of anisotropy it is often not feasible because of drilling and deployment costs. An alternative is to use shear-wave sources on the bottom (e.g. Berge *et al.* 1990) recorded by a multicomponent ocean-bottom seismometer (OBS). Although OBS technology is well advanced, ocean-bottom sources, especially shear-wave sources, are still in an early stage of development. Accordingly it seems worthwhile to examine the feasibility of detecting fracture orientations using surface airgun sources and OBS receivers.

* ANIVEC is a registered trademark of Geo-Pacific Corporation.

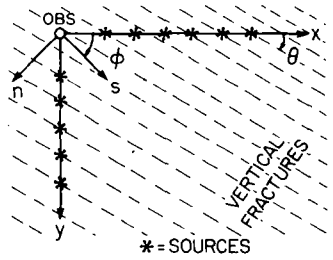

Figure 6. Shooting geometry for multicomponent marine seismic exploration.

Consider a shooting geometry in a realistic marine exploration case, shown in Fig. 6, where we have an OBS with two horizontal components x and y, with the x-direction oriented at an arbitrary angle θ with respect to the strike of the vertical fractures. We now discharge an airgun source near the surface of the water at regular intervals along a line in the x-direction, passing directly above the OBS, and let the x- and y-components of the response recorded by the OBS from these shots be $x_{\parallel}$ and $y_{\parallel}$, respectively. We also discharge the air gun at the same interval along a line in the y-direction, passing directly above the OBS, and let the x- and y-components of OBS response from these shots be $x_{\perp}$ and $y_{\perp}$, respectively. Now in Fig. 6, note that if $\theta = n\pi/2$ (for $n = 0, 1, 2, \ldots$), i.e., if the x-direction is parallel or perpendicular to the strike of the vertical fractures and the y-direction is perpendicular or parallel to the strike of the fractures, the OBS responses $y_{\parallel}$ and $x_{\perp}$ will be identically zero, and the responses $x_{\parallel}$ and $y_{\perp}$ will correspond, respectively, to the propagation directions parallel to and normal to the vertical fractures. As shear waves polarized parallel to the fracture planes are faster than shear waves polarized perpendicular to the fracture planes, it is possible to find the fracture orientation unambiguously from the shear wave arrival times in the $x_{\parallel}$ and $y_{\perp}$ record sections. One is seldom fortunate enough to have $\theta = n\pi/2$; however, the four OBS responses $x_{\parallel}$, $y_{\parallel}$, $x_{\perp}$ and $y_{\perp}$ can be rotated into four new responses $s_{\parallel}$, $n_{\parallel}$, $s_{\perp}$ and $n_{\perp}$, for a new orthogonal pair of receiver directions s and n, oriented at an arbitrary angle ϕ with respect to our (x, y) pair (Fig. 6). This procedure is similar to that used by Alford (1986) for determining fracture direction from shear-wave surface seismic data. The formula for rotation of the seismograms is (Schoenberg *et al.* 1988)

$$\begin{pmatrix} s_{\parallel} \\ n_{\parallel} \\ s_{\perp} \\ n_{\perp} \end{pmatrix} = \mathbf{R} \begin{pmatrix} x_{\parallel} \\ y_{\parallel} \\ x_{\perp} \\ y_{\perp} \end{pmatrix}, \tag{66}$$

where $\mathbf{R}$ is the 4×4 rotation matrix given by

$$\begin{pmatrix} \cos^2\phi & \sin\phi\cos\phi & \sin\phi\cos\phi & \sin^2\phi \\ -\sin\phi\cos\phi & \cos^2\phi & -\sin^2\phi & \sin\phi\cos\phi \\ -\sin\phi\cos\phi & -\sin^2\phi & \cos^2\phi & \sin\phi\cos\phi \\ \sin^2\phi & -\sin\phi\cos\phi & -\sin\phi\cos\phi & \cos^2\phi \end{pmatrix}. \tag{67}$$

We perform this rotation for various values of ϕ. When $\phi = \theta + n\pi/2$ (for $n = 0, 1, 2, 3, \ldots$), the shear arrivals in the near traces of $n_{\parallel}$ and $s_{\perp}$ will vanish, and from the arrival

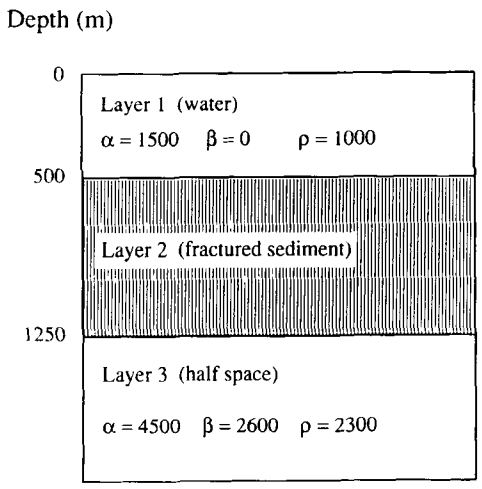

Figure 7. The three-layer marine model used to generate the synthetic seismograms in Figs 8–12. α, β here stand for P- and S-wavespeeds in $m\,s^{-1}$ and ρ stands for density in $kg\,m^{-3}$.

times in the $s_{\|}$ and $n_{\perp}$ sections, we can find the orientation of the vertical fractures.

To demonstrate the rotation technique, we used a three-layer marine model, as described in Fig. 7. The fractured sediment layer in Fig. 7 was generated from a random sequence of two isotropic beds with P-wavespeeds 1800 and 2500 $m\,s^{-1}$, S-wavespeeds 1000 and 1500 $m\,s^{-1}$, densities 1500 and 2000 $kg\,m^{-3}$ and relative proportions 0.5 and 0.5. Following Schoenberg (1983), the resulting medium becomes TI with the following elastic coefficients in units of $10^9\,N\,m^{-2}$: $C_{11}=8.60$, $C_{13}=2.32$, $C_{33}=6.99$, $C_{44}=2.25$, and $C_{66}=3.0$. The density of the composite medium was 1750 $kg\,m^{-3}$. For horizontal propagation, the SH-wavespeed in this medium is 1309 $m\,s^{-1}$ whereas the q_{SV} wavespeed is 1134 $m\,s^{-1}$, a difference of about 15 per cent. Into this TI medium, we then introduced a set of vertical fractures. Following Schoenberg & Douma (1988), this was done by the use of two parameters Z_N and Z_T which are the additional tangential and normal compliances, respectively, due to the fractures, relative to the corresponding compliances of the unfractured medium. With $Z_T=0.02$ and $Z_N=0.01$ (both in $10^{-9}\,m^2\,N^{-1}$), the fractured TI medium became orthorhombic with the following elastic constants (all in $10^9\,N\,m^{-2}$): $C_{11}=7.92$, $C_{12}=2.40$, $C_{13}=2.14$, $C_{22}=8.54$, $C_{23}=2.26$, $C_{33}=6.95$, $C_{44}=2.25$, $C_{55}=2.15$, and $C_{66}=2.83$. The density of the fractured medium remained unchanged. For vertically travelling shear waves, this medium has a wavespeed of 1109 $m\,s^{-1}$ for polarization normal to the fractures, and 1134 $m\,s^{-1}$ for polarization parallel to the fractures, a difference of about 2.25 per cent. Finally we rotated this medium 30° clockwise about the z-axis, so that the x-axis in Fig. 6 makes an angle of $\theta=30°$ with respect to the strike of the vertical fractures.

Figure 8 shows the synthetic seismograms for the marine model described above with sources 10 m deep and OBS sensors 1 m beneath the water bottom. The marked events in these synthetics are: (A) direct arrival, (B) q_P reflection from the top of the isotropic half-space, (C) a doublet of arrivals: q_P–q_{S_1} and q_P–q_{S_2} reflections from the top of the isotropic half space, and (D) four arrivals: q_{S_1}–q_{S_1}, q_{S_1}–q_{S_2}, q_{S_2}–q_{S_1}, and q_{S_2}–q_{S_2} reflections from the top of the isotropic

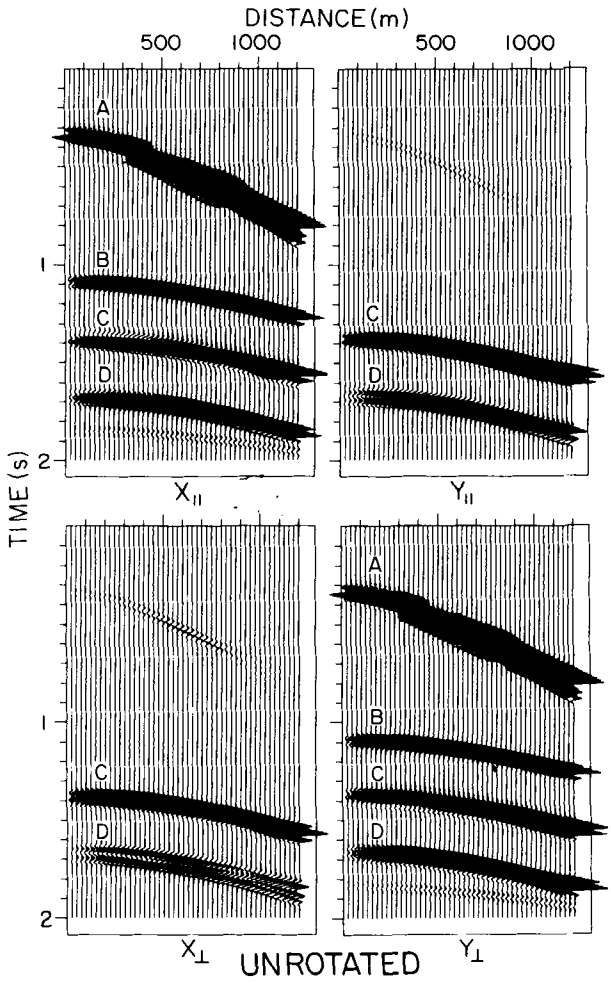

Figure 8. $x_{\|}$, $y_{\|}$, $x_{\perp}$, and $y_{\perp}$ synthetic seismograms computed for the marine model shown in Fig. 7. The source was a surface airgun and the OBS receiver was 1 m beneath the ocean bottom. The arrivals are: (A) direct, (B) q_P reflection from the top of isotropic half-space, (C) a doublet of arrivals: q_P–q_{S_1} and q_P–q_{S_2} reflections from the top of isotropic half-space, (D) four arrivals: q_{S_1}–q_{S_1}, q_{S_1}–q_{S_2}, q_{S_2}–q_{S_1}, and q_{S_2}–q_{S_2} reflections from the top of the isotropic half-space.

half-space. In Figs 9–12, we show the rotated seismograms for $\phi=15°$, 30°, 45°, and 60°, respectively. For $\phi=30°$ (Fig. 10), events C and D vanish from the near traces of $n_{\|}$ and $s_{\perp}$. Also, the arrival times of events C and D are earlier in the $n_{\perp}$ section than in the $s_{\|}$ section in Fig. 10. Therefore at $\phi=30°$, n is the direction parallel to the fractures, and s is the direction perpendicular to the fractures. Note that the reflections are not quelled at larger offsets because at such offsets the shear modes do not have orthogonal polarizations.

As direct shear waves cannot be generated by airguns in the water, our rotation technique will work only if there is conversion to shear at the ocean bottom, or if there are P-to-S reflections from interfaces within the sediment. In most areas of the ocean at least one of these conditions is likely to be satisfied. When an OBS settles at the bottom, the two horizontal components will generally not coincide with the shooting directions, but it is straightforward to determine the orientation of the OBS from the motions of

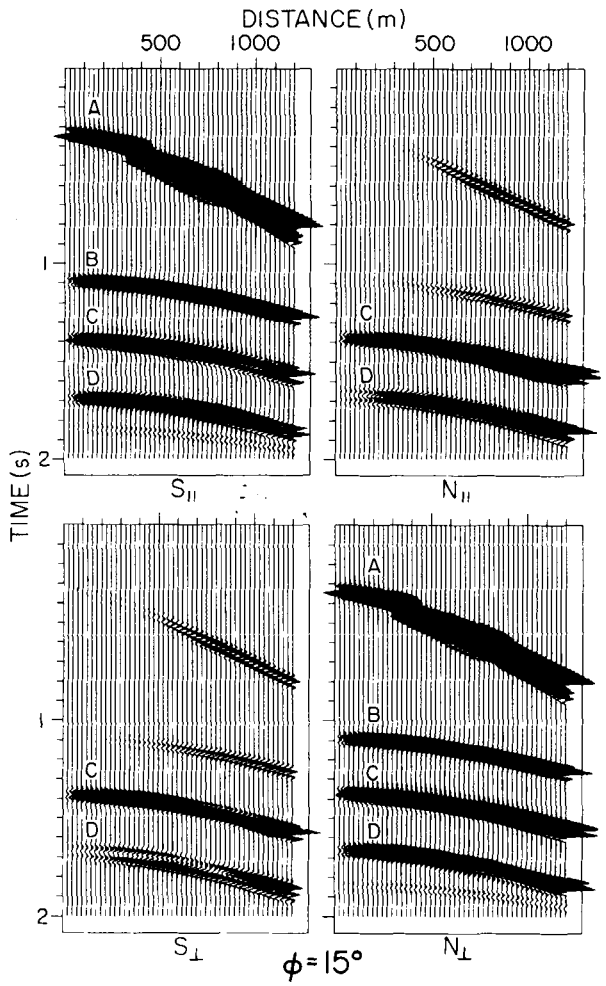

Figure 9. Seismograms obtained from the seismograms of Fig. 7 by rotation through an angle of $\phi = 15°$.

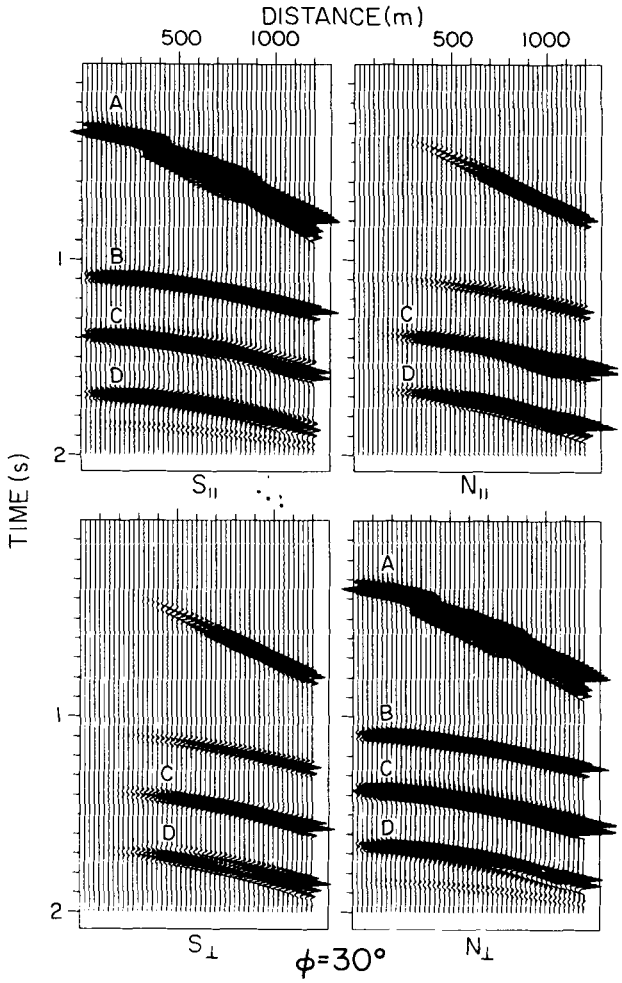

Figure 10. Similar to Fig. 8, but for $\phi = 30°$.

direct arrivals. Although our technique assumes a perfectly flat ocean bottom, in practice one may have different seafloor topography along the two shot lines, causing errors in the rotated seismograms. In the rotation, only very short ranges are important and at these short ranges the undulation in the seafloor is likely to be small. Also it may be possible to correct the data, using time shifts derived from bathymetry, before applying the rotation. The main drawback of the technique of this section is that it requires the deployment of an OBS.

5 FRACTURE ORIENTATION FROM *P*-WAVE SURFACE SEISMIC DATA

As most of our present expertise in analysing and interpreting seismic record sections is for *P*-wave data and as there exists a huge *P*-wave data set from all over the world, it is worthwhile to investigate what information regarding azimuthal anisotropy can be extracted from conventional marine seismic surveys, i.e., from the near-surface pressure response to a near-surface pressure source. To examine this question, we computed synthetic seismograms (not shown) for the four-layer marine model, shown in Fig. 13. In these synthetics the source and receivers were located at the surface of the water layer. The free surface was omitted from the calculations so as to eliminate water bottom multiples. The source spectrum, ray parameter aperture, and numbers of ray parameters, were as given above for Figs 1 and 2. While the top two layers of the model were kept fixed, we varied layers 3 and 4 in the model from isotropic to TI and to AA as outlined in Table 2. With reference to Table 2, the TI models are obtained using Schoenberg (1983) theory for a random sequence of two isotropic beds having *P*-wavespeeds α_1, α_2, *S*-wavespeeds β_1, β_2, densities ρ_1, ρ_2, and relative proportions h_1, h_2. The AA models are obtained from Schoenberg & Douma (1988) theory by introducing sets of vertical fractures with normal and tangential compliances Z_N and Z_T into the TI models.

The isotropic models for layers 3 and 4 (Table 2, column 2) are the simple averages of the respective isotropic sequences (Table 2, column 3) used to generate the TI media.

Figure 14 shows the amplitude versus offset (AVO) plots for the *P*–*P* reflection from the layer 3/layer 4 interface, calculated from the synthetic pressure waveforms at the surface along shooting directions perpendicular to the strike of the fractures, at 45° to the strike of the fractures, and

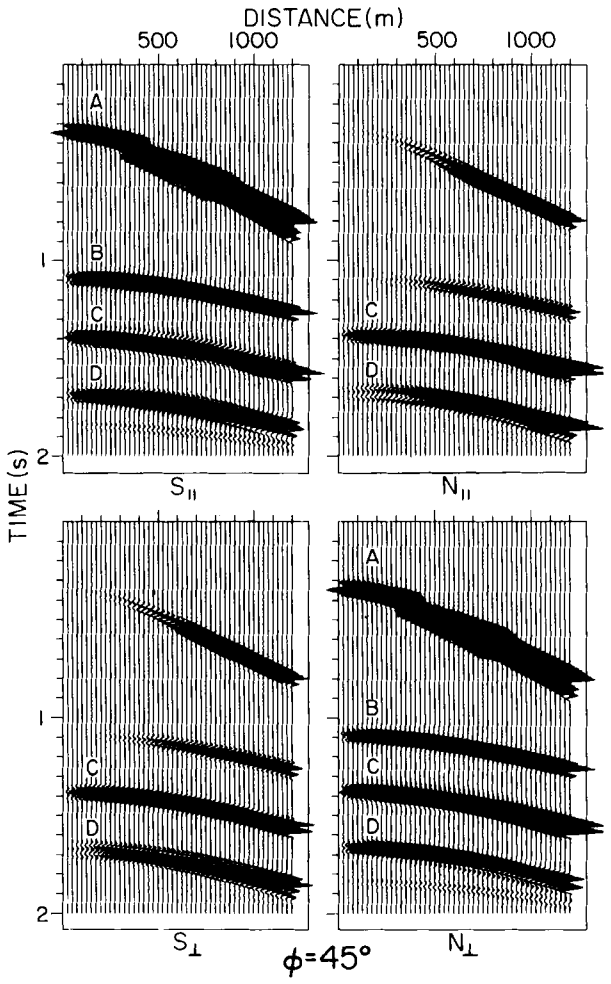

Figure 11. Similar to Fig. 8, but for $\phi = 45°$.

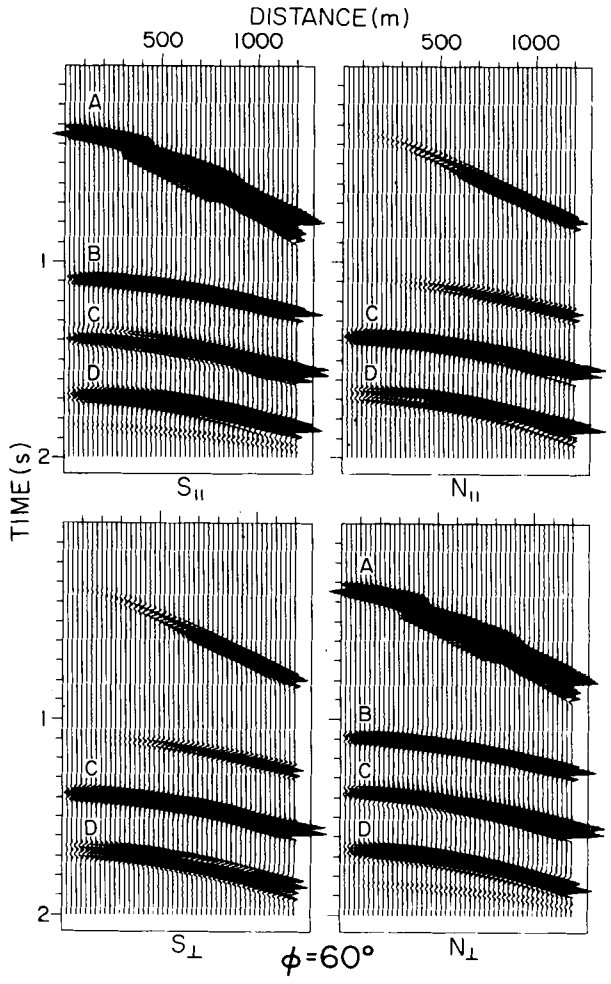

Figure 12. Similar to Fig. 8, but for $\phi = 60°$.

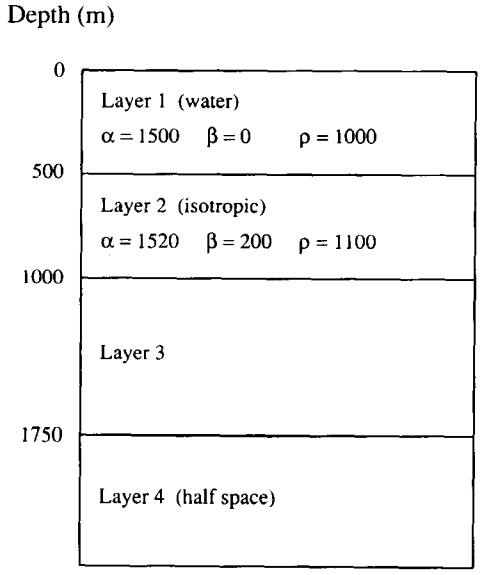

Figure 13. Schematic four-layer marine model used to generate the AVO plots shown in Fig. 14. α, β here stand for *P*- and *S*-wavespeeds in $m\,s^{-1}$ and ρ stands for density in $kg\,m^{-3}$.

Table 2. Properties of the isotropic (ISO), TI, and AA layers 3 and 4 used in the model shown in Fig. 13. Velocities are in $m\,s^{-1}$, densities are in $kg\,m^{-3}$, and the compliances Z_N and Z_T are in $10^{-9}\,m^2\,N^{-1}$.

Layer No.	ISO Model	TI Model	AA Model
3	$\alpha = 2150$ $\beta = 1250$ $\rho = 1750$	$\alpha_1 = 1800$ $\alpha_2 = 2500$ $\beta_1 = 1000$ $\beta_2 = 1500$ $\rho_1 = 1500$ $\rho_2 = 2000$ $h_1 = 0.5$ $h_2 = 0.5$	$Z_N = 0.01$ $Z_T = 0.02$ on TI model background
4	$\alpha = 4500$ $\beta = 2600$ $\rho = 2300$	$\alpha_1 = 4100$ $\alpha_2 = 4900$ $\beta_1 = 2300$ $\beta_2 = 2900$ $\rho_1 = 2050$ $\rho_2 = 2550$ $h_1 = 0.5$ $h_2 = 0.5$	$Z_N = 0.01$ $Z_T = 0.02$ on TI model background

parallel to the strike of the fractures. To make the AVO plots in Fig. 14 we first computed instantaneous amplitude traces from the synthetic waveforms (e.g. Yilmaz 1987). The instantaneous amplitude of the *P*–*P* reflection from the layer 3/layer 4 boundary was then measured, corrected for spherical spreading and plotted as a function of offset. For real data such amplitudes may be uncertain, since in many instances reflections interfere with one another and therefore it may be difficult to estimate the amplitude of one

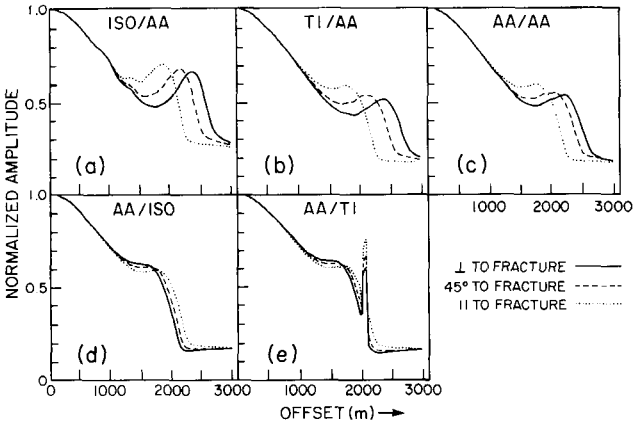

Figure 14. *Amplitude versus offset for the P–P reflection from the* layer 3/layer 4 interface of the four-layer model shown in Fig. 13 and Table 2, (a) layer 3 isotropic and layer 4 AA, (b) layer 3 TI and layer 4 AA, (c) layer 3 AA and layer 4 AA, (d) layer 3 AA and layer 4 isotropic, and (e) layer 3 AA and layer 4 TI.

particular reflection event from the record sections. This difficulty could be overcome by slant stacking (e.g. Phinney, Chowdhury & Frazer 1980), but for the model of Fig. 13 interference was not a problem and slant stacking was unnecessary.

The models used to compute the AVO plots shown in Fig. 14 are: (a) layer 3 isotropic and layer 4 AA, (b) layer 3 TI and layer 4 AA, (c) layers 3 and 4 both AA, (d) layer 3 AA and layer 4 isotropic, and (e) layer 3 AA and layer 4 TI. Fig. 14 demonstrates that *P*-wave reflection AVO is a good indicator of azimuthal anisotropy. Comparison of the different AVO curves indicates the following.

(1) Although the AVO characteristics along the three shooting directions are similar for near-normal reflections (small offsets), they differ significantly for wide-angle reflections (large offsets).

(2) In each AVO plot in Fig. 14, there are distinct peaks in the curves which occur between the offsets 1500–2500 m. These peaks correspond to critical reflections.

(3) When layer 4 is AA (Fig 14a–c), for pre-critical reflections the line parallel to the fractures has higher amplitudes than the line perpendicular to the fractures, whereas for post-critical reflections the line perpendicular to the fractures has higher amplitudes than the line parallel to the fractures.

(4) When layer 4 is isotropic or TI (Fig. 14d,e), for pre-critical reflections the line perpendicular to the fractures has higher amplitudes than the line parallel to the fractures, whereas for post-critical reflections the line parallel to the fractures has higher amplitudes then the line perpendicular to the fractures.

It is therefore possible to use *P*-wave reflection AVO along different shooting directions to detect azimuthal anisotropy and the orientation of vertical fractures. Since the anisotropy that we have assumed in our model is weak (≈2.5 per cent), we expect this AVO technique to work on real data. Although the scope of this paper is limited to marine seismic applications, and we have demonstrated the AVO technique for a marine seismic case only, we expect a similar technique to work for land data, i.e., surface vertical sources recorded into an array of surface vertical geophones on land. A study of AVO and its application in detecting azimuthal anisotropy in the Austin Chalk formation from land *P*-wave data is now in progress and will be discussed in a subsequent paper. Results similar to those presented in this section have been obtained independently by Corrigan (1990), who also used perturbation theory to analyse the dependence of the *P*-wave reflection coefficient on reflection angle and the azimuth of the line with respect to the strike of the fractures.

6 DISCUSSION

We have derived formulae for the reflection/transmission coefficients at interfaces between liquids and AA solids. Synthetic surface seismic and VSP examples demonstrate the usefulness of these formulae. We also showed that multicomponent OBS data from airgun sources along two shooting directions at right angles to each other can be rotated to detect the orientation of vertical fractures. Finally, we showed that in the presence of vertical fractures *P*-wave AVO depends on the orientation of the shot line with respect to the fractures. Therefore it is possible to use *P*-wave AVO in determining fracture orientation.

Although neither method of fracture detection has yet been tested on field data we suspect that the AVO method (Section 5) will prove to be more robust than the rotation method (Section 4). The rotation method requires that motions from sources at different locations be combined as though they were due to the same source. This may make the rotation method vulnerable to small phase shifts caused by bottom topography or a varying source. Although water bottom multiples were omitted from the synthetics used here we do not expect them to be a major problem in the analysis of data. In fact, as such multiples sample the subbottom twice, their sensitivity to fracture direction should be greater than that of the primary reflections.

ACKNOWLEDGMENTS

The possibility of using *P*-wave AVO in fracture detection was suggested to the second author several years ago by Heloise B. Lynn. We thank Geo-Pacific Corporation for the use of ANIVEC^{TM} software and for permission to publish this paper, and we thank Cray Research Corporation for time on the Cray X-MP and Y-MP. Bill Kamp and Gene Shiles were especially helpful. Support by ONR and NSF of earlier theoretical work is gratefully acknowledged. Eduard Berg, Pat Berge, Gerard Fryer, Bertram Nolte and Ram Sriram kindly read the manuscript. SOEST Contribution No. 2389.

REFERENCES

Aki, K. & Richards, P. G., 1980. *Quantitative Seismology*, vol. 1, W. H. Freeman, San Francisco.

Alford, R. M., 1986. Shear data in the presence of azimuthal anisotropy: Dilley, Texas, *Proc. 56th Ann. Int. Mtg. Soc. Expl. Geophys., Houston, Texas*, pp. 476–479, Society of Exploration Geophysicists, Tulsa, OK.

Auld, B. A., 1973. *Acoustic Fields and Waves in Solids*, two volumes, Wiley, New York.

Bamford, D. & Crampin, S., 1977. Seismic anisotropy—the state of the art, *Geophys. J. Int.*, **49**, 1–8.

Berge, P. A., Mallick, S., Fryer, G. J., Barstow, N., Carter, J. A., Sutton, G. H. & Ewing, J. I., 1990. In-situ measurement of transverse isotropy in shallow-water marine sediments, *Geophys. J. Int.*, **104,** 241–254.

Booth, D. C., Crampin, S. & Chesnokov, E. M., 1987. Preface: Proceedings of the second international workshop on seismic anisotropy, *Geophys. J. Int.*, **91,** 261–263.

Červený, V., 1972. Seismic rays and ray intensities in inhomogeneous anisotropic media, *Geophys. J. Int.*, **29,** 1–13.

Chapman, C. H. & Shearer, P. M., 1988. Ray tracing in azimuthally anisotropic media—II Quasi-shear wave coupling, *Geophys. J. Int.*, **96,** 65–83.

Corrigan, D., 1990. *The effect of Azimuthal Anisotropy on the Variation of Reflectivity with Offset,* presented at Fourth Int. Workshop on Seismic Anisotropy, July 2–6, 1990, Edinburgh, Scotland.

Crampin, S., Chesnokov, E. M. & Hipkin, R. G., 1984. Seismic anisotropy—the state of the art: II, *Geophys. J. Int.*, **76,** 1–16.

Frazer, L. N., 1988. Quadrature of wavenumber integrals, in *Seismological Algorithms,* pp. 279–290, ed. Doornbos, D. J., Academic Press, New York.

Frazer, L. N., 1990. Dynamic elasticity of microbedded and fractured rocks, *J. geophys. Res.*, **95,** 8513–8526.

Frazer, L. N. & Fryer, G. J., 1989. Useful properties of the system matrix for a homogeneous anisotropic viscoelastic medium, *Geophys. J. Int.*, **97,** 173–177.

Fryer, G. J. & Frazer, L. N., 1984. Seismic waves in stratified anisotropic media, *Geophys. J. Int.*, **78,** 691–710.

Fryer, G. J. & Frazer, L. N., 1987. Seismic waves in stratified anisotropic media, *Geophys. J. Int.*, **91,** 73–101.

Gajewski, D. & Pšenčík, I., 1990. Vertical seismic profile synthetics by dynamic ray tracing in laterally varying layered anisotropic structures, *J. geophys. Res.*, **95,** 11 301–11 315.

Hudson, J. A., 1980. Overall properties of a cracked solid, *Math. Proc. Cambridge Phil. Soc.*, **88,** 371–384.

Hudson, J. A., 1981, Wave speeds and attenuation of elastic waves in material containing cracks, *Geophys. J. Int.*, **64,** 133–150.

Hudson, J. A., 1986. A higher order approximation to the wave propagation constants for a cracked solid, *Geophys. J. Int.*, **87,** 265–274.

Hudson, J. A., 1988. Seismic propagation through material containing partially saturated cracks, *Geophys. J. Int.*, **92,** 33–37.

Hudson, J. A., 1990a. Overall elastic properties of isotropic materials with arbitrary distribution of circular cracks, *Geophys. J. Int.*, **102,** 465–469.

Hudson, J. A., 1990b. Attenuation due to second-order scattering in material containing cracks, *Geophys. J. Int.*, **102,** 485–490.

Kennett, B. L. N., 1983. *Seismic Wave Propagation in Stratified Media,* Cambridge University Press, Cambridge, UK.

Leary, P. C., Crampin, S. & McEvilly, T. V., 1990. Seismic fracture anisotropy in the earth's crust: an overview, *J. geophys. Res.*, **95,** 11 105–11 114.

Mallick, S. & Frazer, L. N., 1987. Practical aspects of reflectivity modeling, *Geophysics,* **52,** 1355–1364.

Mallick, S. & Frazer, L. N., 1988. Rapid computation of multi-offset vertical seismic profile synthetic seismograms for layered media, *Geophysics,* **53,** 479–491.

Mallick, S. & Frazer, L. N., 1990. Computation of synthetic seismograms for stratified azimuthally anisotropic media, *J. geophys. Res.*, **95,** 8513–8526.

Phinney, R. A., Chowdhury, K. R. & Frazer, L. N., 1980. Transformation and analysis of record sections, *J. geophys. Res.*, **86,** 359–377.

Schoenberg, M., 1983. Reflection of elastic waves from periodically stratified media with interfacial slip, *Geophys. Prosp.*, **31,** 265–292.

Schoenberg, M. & Douma, J., 1988. Elastic wave propagation in media with parallel fractures and aligned cracks, *Geophys. Prosp.*, **36,** 571–590.

Schoenberg, M. & Muir, F., 1989. A calculus for finely layered anisotropic media, *Geophysics,* **54,** 581–589.

Schoenberg, M., Mallick, S. & Frazer, L. N., 1988. Synthetic shear VSP's in azimuthally anisotropic media, *Expl. Geophys. (Australia),* **19,** 151–157.

Shearer, P. & Chapman, C. H., 1988. Ray tracing in azimuthally anisotropic media, I, Results for models of aligned cracks in the upper crust, *Geophys. J. Int.*, **96,** 51–64.

Stephen, R. A., 1985. Seismic anisotropy in the upper oceanic crust, *J. geophys. Res.*, **90,** 11 383–11 396.

Winterstein, D. F., 1990. Velocity anisotropy terminology for geophysicists, *Geophysics,* **55,** 1070–1088.

Yilmaz, Ö, 1987. *Seismic Data Processing,* Society of Exploration Geophysicists, Tulsa, OK.